Ultrathin dendrimer–graphene oxide composite film for stable cycling lithium–sulfur batteries

Wen Liu[a,1], Jianbing Jiang[a,1], Ke R. Yang[a,1], Yingying Mi[a,b,1], Piranavan Kumaravadivel[c], Yiren Zhong[a], Qi Fan[a,2], Zhe Weng[a], Zishan Wu[a], Judy J. Cha[c,d], Henghui Zhou[b], Victor S. Batista[a,3], Gary W. Brudvig[a,3], and Hailiang Wang[a,3]

[a]Department of Chemistry and Energy Sciences Institute, Yale University, West Haven, CT 06516; [b]College of Chemistry and Molecular Engineering, Peking University, Beijing 100871, China; [c]Department of Mechanical Engineering and Materials Science, Yale University, New Haven, CT 06511; and [d]Center for Research on Interface Structures and Phenomena, Yale University, New Haven, CT 06511

Edited by Hongjie Dai, Stanford University, Stanford, CA, and approved February 17, 2017 (received for review December 18, 2016)

Lithium–sulfur batteries (Li–S batteries) have attracted intense interest because of their high specific capacity and low cost, although they are still hindered by severe capacity loss upon cycling caused by the soluble lithium polysulfide intermediates. Although many structure innovations at the material and device levels have been explored for the ultimate goal of realizing long cycle life of Li–S batteries, it remains a major challenge to achieve stable cycling while avoiding energy and power density compromises caused by the introduction of significant dead weight/volume and increased electrochemical resistance. Here we introduce an ultrathin composite film consisting of naphthalimide-functionalized poly(amidoamine) dendrimers and graphene oxide nanosheets as a cycling stabilizer. Combining the dendrimer structure that can confine polysulfide intermediates chemically and physically together with the graphene oxide that renders the film robust and thin (<1% of the thickness of the active sulfur layer), the composite film is designed to enable stable cycling of sulfur cathodes without compromising the energy and power densities. Our sulfur electrodes coated with the composite film exhibit very good cycling stability, together with high sulfur content, large areal capacity, and improved power rate.

lithium–sulfur battery | ultrathin composite film | dendrimer | graphene oxide | long cycle

High-energy-density batteries are demanded for electric transportation and stationary energy storage. Developing such a new generation of batteries requires novel electrode (cathode and anode) materials. Whereas lithium-ion batteries are widely used nowadays in portable electronics and consumer products, further increasing their energy density is a grand challenge as the state-of-the-art cathode materials based on Li^+ intercalation mechanisms (e.g., $LiCoO_2$, $LiFePO_4$, and $LiMn_2O_4$) are approaching their capacity limits (1, 2). Sulfur, a light and abundant element capable of gaining multiple electrons, is a promising alternative cathode material for high-energy-density rechargeable batteries (i.e., Li–S battery) due to its high theoretical capacity of 1,672 mAh g^{-1} (3–6). However, the cycle life of existing Li–S batteries still suffers from significant capacity loss of their sulfur cathodes during cycling, due to dissolution and migration of the formed lithium polysulfide (LPS) intermediates (Li_2S_x, $4 \leq x \leq 8$) during the battery cycling process (7, 8).

Thus far, confining LPS has been regarded as one of the most effective ways of increasing sulfur electrode cyclability. One major approach features incorporation of polysulfide-confining components in electrode material structures or as bifunctional binders. Various materials such as heteroatom-containing carbons (9–14), metal oxides (15–18), metal sulfides (19, 20), metal–organic complexes (21, 22), and macromolecules containing N or O functional groups (23–25) have demonstrated strong affinity to LPS and consequently cycling stability improvement, although the chemical interaction mechanisms between the electrode surface and LPS in the presence of solvent molecules are still elusive. Another strategy is to insert a polysulfide diffusion barrier interlayer in the battery structure, which separates the polysulfide-confining function from the electrode itself and can thus be applicable to essentially any type of sulfur cathode material. An ideal polysulfide control interlayer should have the following properties: (*i*) strong chemical interactions with LPS in addition to physical confinement to effectively block polysulfide migration to the anode; (*ii*) low thickness and light weight with highly exposed LPS interactive sites to minimize dead volume/weight; (*iii*) low electrochemical resistance to ensure normal working voltage and good rate capability; and (*iv*) well-defined surface site structures to elucidate the LPS binding mechanisms on the molecular level. Whereas a number of interlayer structures based on carbon (26–29), polymers (30), metal foams (31), oxide layers (32), and oxide/carbon composites (33, 34) have been reported in the literature, they fall short in one or more of these aspects (*SI Appendix*, Table S1).

In this work, we develop a composite thin film comprising naphthalimide-functionalized poly(amidoamine) (PAMAM) G4 dendrimer (Naph-Den) and mildly oxidized graphene oxide (mGO) as an LPS-confining interlayer to realize high-performance sulfur cathodes that can be stably cycled. In the film structure, the three components have distinct functionalities: the amide-containing dendrimer molecules effectively trap polysulfides via strong chemical binding which is further enhanced by the branched dendrimer structure; the terminal naphthalimide groups attached to the dendrimer structure interact with mGO via π–π stacking and enable composite formation; the mGO nanosheets impart mechanical strength and durability to the

Significance

The promise of lithium–sulfur batteries for future electric transportation and stationary energy storage is being limited by their poor cycling stability. Previous approaches to improvement often involve incorporating additional components with significant dead weight or volume in battery structures. We develop an ultrathin functionalized dendrimer–graphene oxide composite film which can be applied to virtually any sulfur cathode to alleviate capacity fading over battery cycling without compromising the energy or power density of the entire battery. The design provides a new strategy for confining lithium polysulfide intermediates and thus stabilizing lithium–sulfur batteries. It also brings a suitable platform for elucidating the underlying materials and surface chemistry.

Author contributions: W.L., J.J., Q.F., and H.W. designed research; W.L., J.J., K.R.Y., Y.M., P.K., Y.Z., Z. Weng, and Z. Wu performed research; P.K. and J.J.C. contributed new reagents/analytic tools; W.L., J.J., K.R.Y., Y.M., Y.Z., Z. Weng, Z. Wu, V.S.B., and G.W.B. analyzed data; and W.L., K.R.Y., H.Z., V.S.B., G.W.B., and H.W. wrote the paper.

The authors declare no conflict of interest.

This article is a PNAS Direct Submission.

[1]W.L., J.J., K.R.Y., and Y.M. contributed equally to this work.

[2]Present address: School of Chemistry and Chemical Engineering, Southeast University, Nanjing, Jiangsu 211189, China.

[3]To whom correspondence may be addressed. Email: hailiang.wang@yale.edu, victor.batista@yale.edu, or gary.brudvig@yale.edu.

This article contains supporting information online at www.pnas.org/lookup/suppl/doi:10.1073/pnas.1620809114/-/DCSupplemental.

100-nm-thick film. The composite film enables a Li–S battery with very good cycling stability and improved rate capability. With a sulfur content of 76 wt % in the electrode material and a sulfur mass loading of 2 mg cm^{-2} on the electrode, the cathode exhibits a capacity decay rate as low as 0.008% per cycle over 500 cycles. As a result of the negligible thickness/weight of the composite film, the battery energy density is hardly affected. The well-defined molecular structure of the dendrimer facilitates mechanistic investigation of LPS binding. X-ray photoelectron spectroscopy (XPS) studies and density-functional theory (DFT) calculations suggest that the Li ions of LPS bind strongly to the O atoms in the amide groups of the dendrimer.

Results

The PAMAM G4 dendrimer was first functionalized by reacting the terminal amine groups with *1,8*-naphthalic anhydride (Fig. 1*A*). Successful decoration was confirmed by UV-vis (*SI Appendix*, Fig. S1) and ^{1}H NMR (*SI Appendix*, Fig. S2) spectra. Mixing the Naph-Den *N,N*-dimethylformamide (DMF) solution with an mGO DMF suspension forms a sticky slurry (Fig. 1*B*) that can be conveniently casted onto substrates using doctor blading to afford a thin film (Fig. 1*C*). The atomic force microscopy (AFM) image shows that the thickness of the film is about 100 nm (Fig. 1*D*). We coated the Naph-Den–mGO slurry onto a prepared GO–S (*SI Appendix*, Fig. S3) electrode surface (Fig. 1*E*). As a proof of concept, the GO–S electrode material had a sulfur content of 65 wt % and the sulfur mass loading on the cathode was 1 mg cm^{-2}. Fig. 1*F* shows the top view of the GO–S electrode coated with the Naph-Den–mGO film (Naph-Den–mGO/GO–S), where a thin surface layer is observed. C, N, O, and S elements are identified by energy-dispersive X-ray spectroscopy (EDX), which confirms the existence of the *N*-containing dendrimer in the surface layer (*SI Appendix*, Fig. S4). Fig. 1*G* shows the side view of the Naph-Den–mGO/GO–S electrode, where the Naph-Den–mGO layer can be clearly distinguished from the underlying GO–S layer. The Naph-Den–mGO film has a thickness of ∼90 nm shown in the enlarged image, which is a negligible fraction (<1%) in volume compared with the active GO–S layer.

The Naph-Den–mGO/GO–S electrode was evaluated in a coin cell with a Li metal anode. The cell was first discharged and recharged at various current rates (0.1–10 C), and then tested for consecutive long-term cycling at 1.0 and 2.0 C. Specific capacities of 1,472, 1,255, 1,083, and 943 mAh g^{-1} (based on sulfur mass) were observed at 0.1, 0.2, 0.5, and 1.0 C together with well-defined voltage profiles (Fig. 2 *A* and *B*). Remarkably, reversible capacities of 785 and 530 mAh g^{-1} were obtained at high rates of 2.0 and 5.0 C (Fig. 2 *A* and *B*). As a comparison, the GO–S cathode without the Naph-Den–mGO film exhibited comparable capacities at low rates but much lower capacities at high rates (Fig. 2*B* and *SI Appendix*, Fig. S5). At 5.0 C the specific capacity was already as low as 143 mAh g^{-1}.

The cell was then cycled at 1.0 C with a starting capacity of 830 mAh g^{-1}. After 560 cycles at 1.0 C, the Naph-Den–mGO/GO–S electrode retained a capacity of 757 mAh g^{-1}, corresponding to an average capacity loss of 0.016% per cycle (Fig. 2*C*). After that the cell was further cycled for another 665 cycles at 2.0 C, during which the capacity dropped from 668 to 562 mAh g^{-1}, giving an average capacity decay of 0.024% per cycle (Fig. 2*C*). Stable charging and discharging voltage profiles with well-defined voltage plateaus were recorded throughout the cycling process (*SI Appendix*, Fig. S6). In comparison, the GO–S cathode without the Naph-Den–mGO film showed inferior cycle life. The capacity decreased 0.054% per cycle at 1.0 C, and then 0.073% per cycle at 2.0 C (Fig. 2 *C* and *D*).

We further increased the sulfur content in the GO–S electrode material to 76 wt % (*SI Appendix*, Fig. S7) and the sulfur mass loading on the electrode to 2 mg cm^{-2}. The Naph-Den–mGO/GO–S electrode still had better kinetics than the GO–S electrode as evidenced by the voltage profiles with flatter discharging plateaus (*SI Appendix*, Fig. S8), although both electrodes manifested compromised specific capacities and rate capabilities as

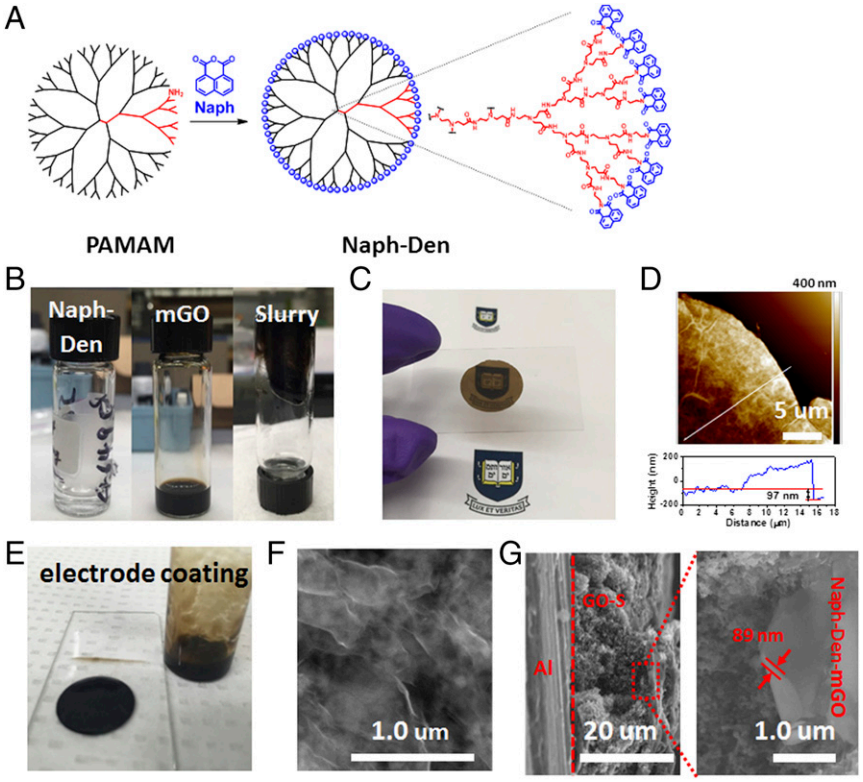

Fig. 1. Illustration of Naph-Den synthesis and sulfur cathode fabrication. (*A*) Molecular structure illustration of Naph-Den. (*B*) Digital photos of Naph-Den DMF solution, mGO DMF suspension, and Naph-Den–mGO slurry. (*C*) A thin Naph-Den–mGO film on a glass slide, prepared by casting the slurry on copper foil and then transferring the film. (*D*) AFM image and height profile for the Naph-Den–mGO film, showing an average thickness of 97 nm with thicker folded edges. (*E*) Digital photo of a GO–S electrode coated with the Naph-Den–mGO layer. (*F*) SEM image of the surface of the Naph-Den–mGO/GO–S electrode. (*G*) SEM side views of the Naph-Den–mGO/GO–S electrode, with the enlarged image showing the thickness of the Naph-Den–mGO film.

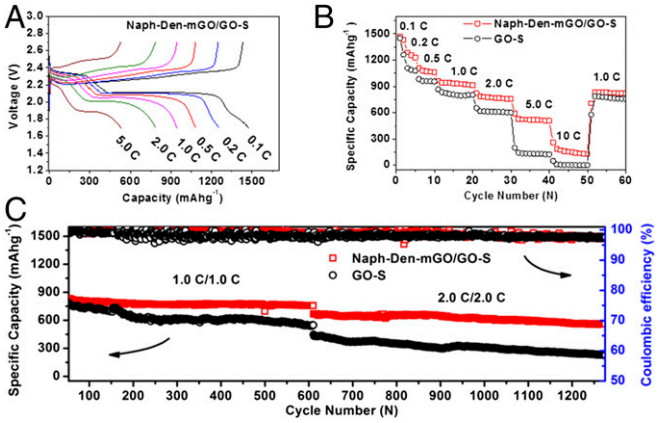

Fig. 2. Electrochemical performance of the Naph-Den-mGO/GO-S electrode compared with the GO–S electrode. (*A*) Representative discharging and charging voltage profiles for the Naph-Den–mGO/GO–S electrode at various rates. (*B*) Discharging specific capacities at various rates. (*C*) Cycling stability for 560 cycles at 1.0 C and consecutive 665 cycles at 2.0 C. The GO–S electrode material has a sulfur content of 65 wt %, and the sulfur mass loading on the cathode is 1 mg cm^{-2}.

the sulfur content and mass loading increased. Notably, the Naph-Den–mGO/GO–S electrode still exhibited excellent cycling stability. Starting from 727 mAh g^{-1} at 1.0 C, the capacity remained 698 mAh g^{-1} after 500 cycles, giving an average capacity loss as low as 0.008% per cycle (Fig. 3*A*). Importantly, the discharge voltage did not decay over the 500 cycles (Fig. 3*B*). Without the Naph-Den–mGO film, the GO–S electrode experienced much faster capacity decay (0.068% per cycle) accompanied by decreasing discharging voltages (Fig. 3 *A* and *C*). Parallel testing demonstrated consistency in electrochemical performance of the Naph-Den–mGO/GO–S cathodes. Capacity decay of about 0.01% per cycle over 1,000 discharging–recharging cycles can be realized (*SI Appendix*, Fig. S9). As sulfur mass loading further increased to 3.5 mg cm^{-2}, the Naph-Den–mGO/GO–S electrode was able to deliver a stable specific capacity of ∼1,000 mAh g^{-1} at 0.2 C, corresponding to a high areal capacity of 3.5 mAh cm^{-2} (*SI Appendix*, Fig. S10). At 0.5 C, ∼750 mAh g^{-1} and 2.8 mAh cm^{-2} could be achieved with negligible capacity fading over cycling (*SI Appendix*, Fig. S11). The Naph-Den–mGO film can also enhance cycling performance of other sulfur electrodes. Protected by the composite film, a carbon nanotube buckypaper electrode loaded with 6 mg cm^{-2} of sulfur exhibited stable capacity of ∼750 mAh g^{-1} at 0.5 C (*SI Appendix*, Fig. S12).

Electrochemical impedance spectroscopy (EIS) was performed for the Naph-Den–mGO/GO–S and GO–S electrodes before and after long-term cycling. The Nyquist plots are shown in Fig. 4*A*. Typically the depressed semicircle in the high-to medium-frequency region reflects charge transfer resistance (R_{ct}) and the inclined line in the low-frequency region is related to mass transfer process (35, 36). The GO–S cathode had an initial R_{ct} of 25 Ω, which rose to 175 Ω after 1,275 discharging–charging cycles. Applying the Naph-Den–mGO film drastically suppresses the increase of charge transfer resistance over cycling. The R_{ct} of the Naph-Den–mGO/GO–S cathode only increased to 45 Ω from the initial 32 Ω over 1,275 cycles. The Naph-Den–mGO/GO–S electrode after long-term cycling was imaged with SEM. The surface of the cycled electrode remained smooth and clean without chunk precipitates (Fig. 4*B*). The EDX spectrum (*SI Appendix*, Fig. S13) revealed C, N, O, F, and S elements on the electrode surface, which indicated the robustness of the Naph-Den–mGO film. The side-view image of the cycled electrode further confirmed the integrity of the surface film over cycling (Fig. 4*C*). It was observed that the thickness of the film increased to 400 nm due to uptake of sulfur species during the cycling process. The elemental distributions of C and S in the vertical cross-section of the electrode are shown in Fig. 4*D*. It is clear that the sulfur species are well confined by the surface film. The electrochemical stability of the composite film was also verified by cyclic voltammetry (CV) measurements: In the potential window of 1.7–2.7 V vs. Li^+/Li (the operating voltage range of sulfur cathodes), the film showed no obvious redox peaks during repeated CV cycles (*SI Appendix*, Fig. S14).

To further examine the LPS-confining effect of the Naph-Den–mGO film, Li | GO–S and Li | Naph-Den–mGO/GO–S cells were disassembled after 250 cycles, and the used Li anodes were carefully analyzed with SEM and EDS. From the digital photos of the disassembled cells (*SI Appendix*, Fig. S15 *A* and *B*), it is obvious that the separator of the cycled Li | GO–S cell contains a significant amount of LPS (yellow), whereas the separator of the cycled Li | Naph-Den–mGO/GO–S cell is almost free of LPS. Combined SEM imaging and EDS mapping (*SI Appendix*, Figs. S15–17) shows that the cycled Li anode paired with the GO–S cathode is composed of loosely packed small Li particles with a high amount of sulfur species, whereas that paired with the Naph-Den–mGO/GO–S cathode features densely packed, larger Li granules containing a much smaller amount of sulfur. These data, taken together, reveal that the shuttle effect has been substantially suppressed by deploying the Naph-Den–mGO interlayer.

The polysulfide-confining Naph-Den–mGO film promotes high electrochemical performance of sulfur cathodes. The composite film not only prevents LPS from diffusing away from the cathode and thus avoids active material loss and Coulombic efficiency decrease, but it also affords a uniform environment on the cathode surface for facile LPS redox conversion and thus ensures a high degree of utilization of active material and low electrochemical resistance throughout the long-term cycling process. As a result, the Naph-Den–mGO/GO–S electrode has a long cycle life with a capacity decay of <0.01% per cycle, which substantially outperforms any other sulfur cathode with interlayer protection (*SI Appendix*, Table S1). It is also arguably the best cycling stability among all sulfur cathodes reported to date (*SI Appendix*, Table S2). It is worth mentioning that our

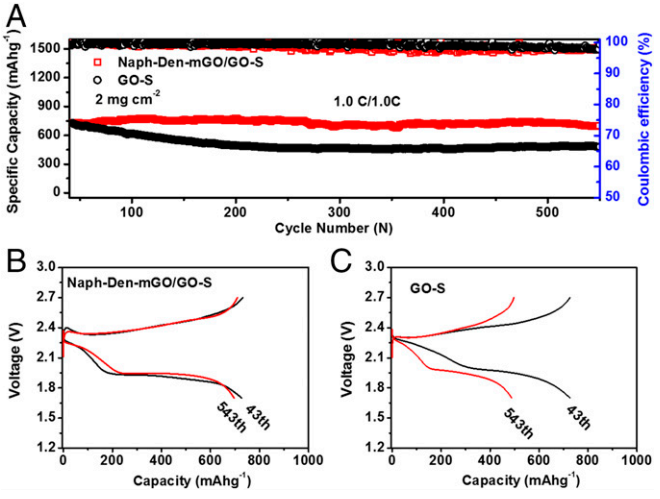

Fig. 3. Electrochemical performance of the Naph-Den–mGO/GO–S electrode with higher sulfur content and mass loading. (*A*) Cycling performance at 1.0 C. (*B*) Discharging–charging voltage profiles of the Naph-Den–mGO/GO–S electrode before and after 500 cycles at 1.0 C. (*C*) Discharging–charging voltage profiles of the GO–S electrode before and after 500 cycles at 1.0 C. The GO–S electrode material has a sulfur content of 76 wt %, and the sulfur mass loading on the cathode is 2 mg cm^{-2}.

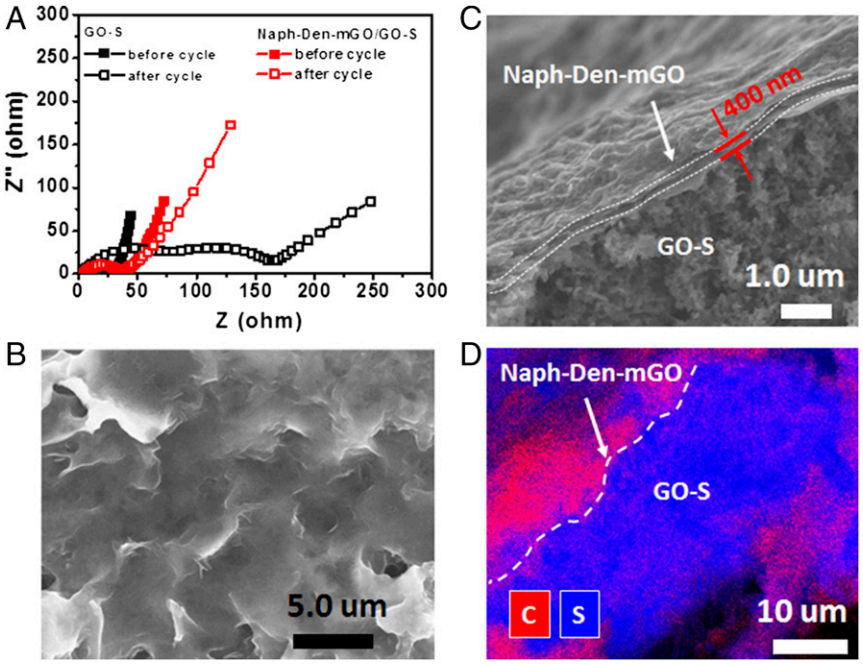

Fig. 4. Characterizations of the Naph-Den-mGO/GO-S electrode after long-term cycling. (*A*) Nyquist plots of the EIS spectra of the Naph-Den–mGO/GO–S cathode measured at 2.4 V before and after 1,275 cycles, in comparison with the GO–S cathode. (*B*) Top-view SEM image of the cycled electrode. (*C*) Side-view SEM image of the cycled electrode. (*D*) EDX elemental mapping of the vertical cross-section of the cycled electrode.

Naph-Den–mGO film is only 100 nm thick; its small volume and light weight allow for cycling stability enhancement without compromising the battery energy and power densities. This is difficult to achieve with previously reported interlayers that are usually thicker or heavier by at least one order of magnitude (*SI Appendix*, Fig. S18). With *N*- and O-containing functional groups embedded in its branched structure, the Naph-Den is expected to interact with LPS strongly. In a control experiment, we evaluated a GO–S electrode coated with an mGO film without the dendrimer component. The capacity fading over cycling (0.049% per cycle) was substantially faster than the Naph-Den–mGO/GO–S electrode, although slightly slower than the GO–S electrode without any film coated (*SI Appendix*, Fig. S19). It is thus clear that the Naph-Den is the central component of the composite film for confining polysulfides. The following part of the article will discuss the molecular origins of the binding between the Naph-Den and LPS.

Discussion

We first used XPS to probe the chemical interactions between Naph-Den and LPS using Li_2S_4 as a model compound. The S 2p core-level spectrum of Li_2S_4 exhibits two sets of doublets located at 163.1/164.3 eV and 161.4/162.6 eV (Fig. 5*A*), with binding energy splittings of 1.2 eV, which are attributed to the bridging and terminal sulfur (S_B^0 and S_T^{-1}) atoms, respectively. The spectral features agree well with previous results reported elsewhere (37). In the presence of Naph-Den, the S 2p doublets both shift to lower binding energy (Fig. 5*A*), indicating increased valence electron density on the S atoms upon interaction with Naph-Den. The binding energy of the N 1s electrons in the Naph-Den remains almost unchanged upon interaction with Li_2S_4 (Fig. 5*B*), which suggests a minor contribution from the N sites in the dendrimer structure for LPS binding. This is distinct from previous reports where N atoms in the carbon materials bind LPS strongly (14). The O 1s spectrum of Naph-Den exhibits two components at 531.8 and 533.5 eV (Fig. 5*C*), which could be due to the O atoms of the amide and imide groups in the Naph-Den structure. In the presence of Li_2S_4, the O 1s peak shifts to lower binding energy, indicating that the O atoms interact strongly with LPS. Further XPS studies reveal that the PAMAM dendrimer interacts with Li_2S_4 in a similar manner as the Naph-Den (*SI Appendix*, Fig. S20). It is thus likely that the O atoms of the amide groups in the PAMAM structure are the major interactive sites responsible for Naph-Den binding with LPS.

We then performed DFT calculations to examine the LPS binding mechanism. We modeled LPS with LiSSH to include S atoms representing both the terminal and bridging S atoms in LPS. Different from many previous reports based on binding energy (ΔE_B) (14, 23), we focused on the binding free energy (ΔG_B) to evaluate the interaction strength between LiSSH and different binding sites (BSite) and/or solvent molecules (Sol). ΔG_B is defined as follows:

$$\Delta G_B = G(\mathrm{HSSLiSol}_m\mathrm{BSite}_n) - G(\mathrm{HSSLi}) - mG(\mathrm{Sol}) - nG(\mathrm{BSite}),$$

where $\mathrm{HSSSLiSol_mBSite_n}$ is the complex of LiSSH with m solvent molecules and n binding sites. The use of ΔG_B in place of ΔE_B brings the advantage of including both thermal and entropy corrections, which is important for accurate modeling of the interaction strength. For example, we calculated the ΔE_B of LiSSH to the 1,3-dioxolane (DOL) solvent molecule to be −20.7 kcal mol^{-1} (*SI Appendix*, Fig. S21), in excellent agreement with previously reported values for similar systems (14, 38). However, taking entropy into consideration, ΔG_B for binding of LiSSH to DOL is −10.6 kcal mol^{-1}, which differs substantially from ΔE_B. We found that ΔG_B for binding of LiSSH to another solvent molecule, dimethoxyethane (DME), is −20.6 kcal mol^{-1}, significantly more negative than that for DOL (Fig. 6 *A* and *B*), suggesting that LiSSH prefers to be solvated by the chelating ligand DME. ΔG_B for binding of LiSSH to two DME molecules is −24.3 kcal mol^{-1} (Fig. 6*C*), corresponding to ΔG of −3.7 kcal mol^{-1} for HSSLi-DME to bind a second DME molecule. Therefore, LiSSH prefers to be solvated by two DME molecules in the battery electrolyte, consistent with previous reports on DME-solvated Li complexes in both solution (39) and crystals (40, 41).

Now we turn to the binding of LiSSH to Naph-Den. There are three sites in the Naph-Den molecular structure that can bind LPS, namely the O atoms in the amide groups (O1 site), the N atoms in the tertiary amine groups (N1 site), and the O atoms in the terminal imide groups (Ot site), as shown in *SI Appendix*, Fig. S22. *SI Appendix*, Fig. S23 shows that the binding between LiSSH and a functional group is hardly affected by other atoms beyond

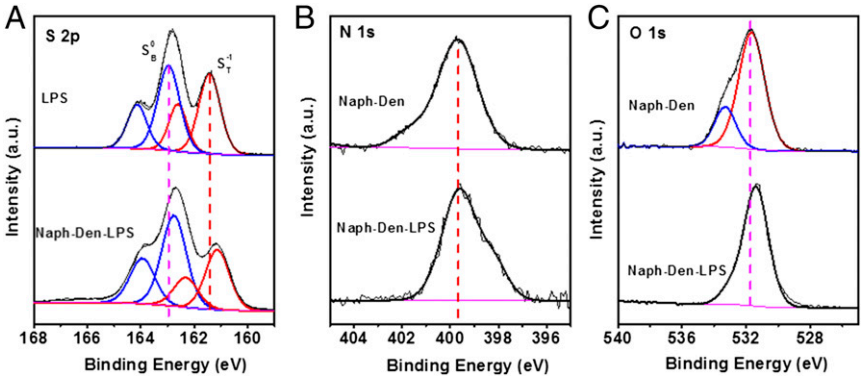

Fig. 5. XPS analysis of the interactions between Naph-Den and LPS. (*A*) S 2p core-level spectra of Li_2S_4 before and after interacting with Naph-Den. (*B*) N 1s and (*C*) O 1s core-level spectra of Naph-Den before and after interacting with Li_2S_4.

the functional group, and thus demonstrates the validity of our model. As shown in Fig. 6 *D–F*, ΔG_B values for binding of LiSSH to the N1, O1, and Ot sites in Naph-Den are −13.2, −19.0, and 17.3 kcal mol^{-1}, respectively. All are smaller than that to DME, indicating that the three types of binding sites are unlikely to replace the DME ligand in HSSLi(DME). ΔG_B values for binding of LiSSH to the N1, O1, and Ot sites in the presence of one DME molecule are calculated to be −22.8, −27.0, and −24.5 kcal mol^{-1}, respectively (Fig. 6 *G–I*). The ΔG_B values for binding of HSSLi(DME) to the N1, O1, and Ot sites can thus be derived to be −1.2, −6.4, and −3.9 kcal mol^{-1}, respectively. Compared with the ΔG_B values for binding of HSSLi(DME) to a second DME molecule (−3.7 kcal mol^{-1}), our results suggest that it is thermodynamically favorable for the O1 site to replace a DME molecule in $HSSLi(DME)_2$ (ΔG = −2.7 kcal mol^{-1}) and thus bind LPS. Our results also suggest that the N1 site is unlikely to bind the solvated LiSSH.

Considering that the samples for XPS study are under high vacuum condition in which the volatile organic solvents are likely to be removed from the samples, we include analysis of interactions

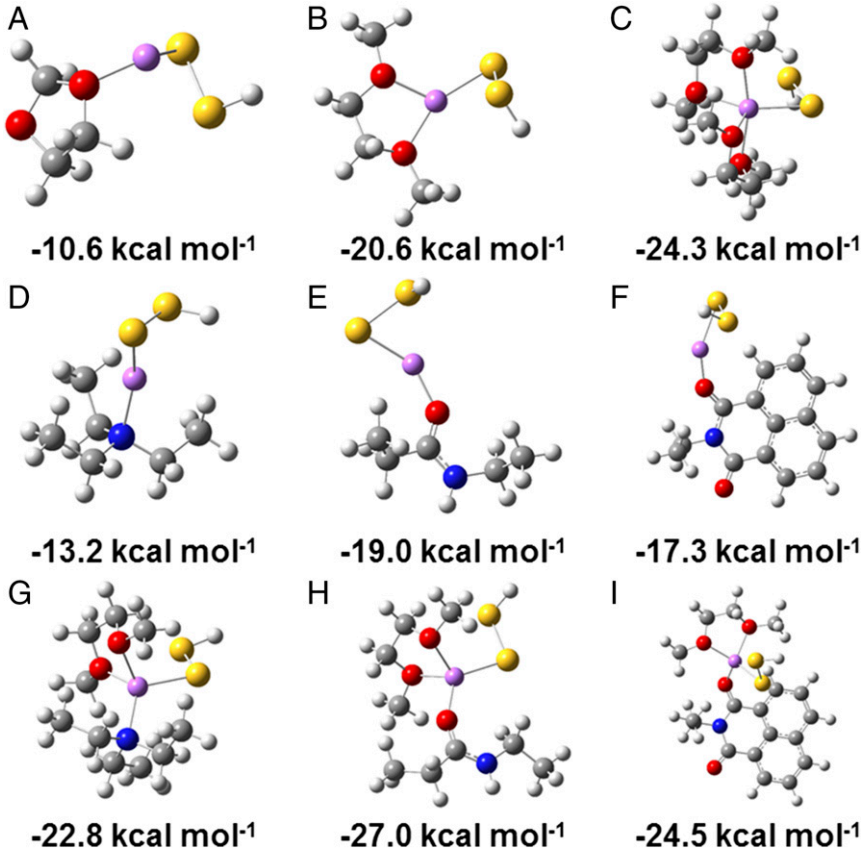

Fig. 6. DFT calculations of binding free energies (ΔG_B). Optimized geometries for the binding of LiSSH to (*A*) one DOL molecule, (*B*) one DME molecule, (*C*) two DME molecules, (*D*) N1 site, (*E*) O1 site, (*F*) Ot site, (*G*) N1 site and one DME molecule, (*H*) O1 site and one DME molecule, and (*I*) Ot site and one DME molecule, and corresponding binding free energies in kilocalorie per mole. Gray, white, red, blue, yellow, and purple balls represent C, H, O, N, S, and Li atoms, respectively.

between LiSSH and Naph-Den in the absence of solvent molecules. The calculated binding free energies suggest that the O1 site should still be the dominant binding sites for LPS (*SI Appendix*, Fig. S24 *A–C*). Based on the optimized structure for LiSSH binding to the O1 site of the Naph-Den, we further calculated the partial atomic charges for the S, O, and N atoms in the structure to correlate with the binding energy shifts measured by XPS (42, 43). As shown in *SI Appendix*, Fig. S24*D*, the Mulliken charges on the O atom of the Naph-Den O1 site and on the S atoms of the LiSSH all become more negative (with increased electron density) upon interaction, which well explains the experimentally observed red shifts of O 1s and S 2p binding energies in the XPS spectra. It is, therefore, confirmed that the O atoms of the amide groups in the Naph-Den structure are the dominant sites that bind LPS.

In summary, we have designed and developed an ultrathin dendrimer–GO composite film to mitigate the polysulfide shuttling problem and stabilize the cycling of Li–S batteries without compromising their energy and power densities. The dendrimer molecules provide strong affinity to polysulfides via specific chemical interactions between amide groups and Li ions. The graphene oxide nanosheets ensure mechanical robustness and low thickness. The resulting combination of materials leads to a composite film interlayer with unique properties and outstanding performance, opening a viable and effective strategy to afford high-performance cathodes for Li–S batteries.

Materials and Methods

Material synthesis, electrode preparation, materials characterization, electrochemical measurements, and computational methods are detailed in *SI Appendix*.

ACKNOWLEDGMENTS. K.R.Y. and V.S.B. acknowledge computer time from the National Energy Research Scientific Computing Center and the Yale High Performance Computation Center. This work was partially supported by Yale University. Y.M. acknowledges the support from China Scholarship Council. Computational and synthetic work was supported by the US Department of Energy Office of Science, Office of Basic Energy Sciences, under Award DE-FG02-07ER15909 and by a generous donation from the TomKat Charitable Trust.

1. Manthiram A (2011) Materials challenges and opportunities of lithium ion batteries. *J Phys Chem Lett* 2(3):176–184.
2. Choi NS, et al. (2012) Challenges facing lithium batteries and electrical double-layer capacitors. *Angew Chem Int Ed Engl* 51(40):9994–10024.
3. Bruce PG, Freunberger SA, Hardwick LJ, Tarascon JM (2011) Li-O_2 and Li-S batteries with high energy storage. *Nat Mater* 11(1):19–29.
4. Manthiram A, Fu Y, Su YS (2013) Challenges and prospects of lithium-sulfur batteries. *Acc Chem Res* 46(5):1125–1134.
5. Seh ZW, Sun Y, Zhang Q, Cui Y (2016) Designing high-energy lithium-sulfur batteries. *Chem Soc Rev* 45(20):5605–5634.
6. Pang Q, Liang X, Kwok CY, Nazar LF (2016) Advances in lithium–sulfur batteries based on multifunctional cathodes and electrolytes. *Nat Energy* 1:16132.
7. Mikhaylik YV, Akridge JR (2004) Polysulfide shuttle study in the Li/S battery system. *J Electrochem Soc* 151:A1969–A1976.
8. Sun Y, et al. (2015) In-operando optical imaging of temporal and spatial distribution of polysulfides in lithium-sulfur batteries. *Nano Energy* 11:579–586.
9. Wang H, et al. (2011) Graphene-wrapped sulfur particles as a rechargeable lithium-sulfur battery cathode material with high capacity and cycling stability. *Nano Lett* 11(7):2644–2647.
10. Ji L, et al. (2011) Graphene oxide as a sulfur immobilizer in high performance lithium/sulfur cells. *J Am Chem Soc* 133(46):18522–18525.
11. Wang Z, et al. (2014) Enhancing lithium-sulphur battery performance by strongly binding the discharge products on amino-functionalized reduced graphene oxide. *Nat Commun* 5:5002.
12. Peng H-J, et al. (2014) Strongly coupled interfaces between a heterogeneous carbon host and a sulfur-containing guest for highly stable lithium-sulfur batteries: Mechanistic insight into capacity degradation. *Adv Mater Interfaces* 1(7):1400227.
13. Song J, et al. (2014) Nitrogen-doped mesoporous carbon promoted chemical adsorption of sulfur and fabrication of high-areal-capacity sulfur cathode with exceptional cycling stability for lithium-sulfur batteries. *Adv Funct Mater* 24(9):1243–1250.
14. Zhou G, Paek E, Hwang GS, Manthiram A (2015) Long-life Li/polysulphide batteries with high sulphur loading enabled by lightweight three-dimensional nitrogen/sulphur-codoped graphene sponge. *Nat Commun* 6:7760.
15. Wei Seh Z, et al. (2013) Sulphur-TiO_2 yolk-shell nanoarchitecture with internal void space for long-cycle lithium-sulphur batteries. *Nat Commun* 4:1331.
16. Pang Q, Kundu D, Cuisinier M, Nazar LF (2014) Surface-enhanced redox chemistry of polysulphides on a metallic and polar host for lithium-sulphur batteries. *Nat Commun* 5:4759.
17. Fan Q, Liu W, Weng Z, Sun Y, Wang H (2015) Ternary hybrid material for high-performance lithium-sulfur battery. *J Am Chem Soc* 137(40):12946–12953.
18. Tao X, et al. (2016) Balancing surface adsorption and diffusion of lithium-polysulfides on nonconductive oxides for lithium-sulfur battery design. *Nat Commun* 7:11203.
19. Seh ZW, et al. (2014) Two-dimensional layered transition metal disulphides for effective encapsulation of high-capacity lithium sulphide cathodes. *Nat Commun* 5:5017.
20. Yuan Z, et al. (2016) Powering lithium-sulfur battery performance by propelling polysulfide redox at sulfiphilic hosts. *Nano Lett* 16(1):519–527.
21. Demir-Cakan R, et al. (2011) Cathode composites for Li-S batteries via the use of oxygenated porous architectures. *J Am Chem Soc* 133(40):16154–16160.
22. Zhou J, et al. (2014) Rational design of a metal-organic framework host for sulfur storage in fast, long-cycle Li-S batteries. *Energy Environ Sci* 7(8):2715–2724.
23. Seh ZW (2013) Stable cycling of lithium sulfide cathodes through strong affinity with a bifunctional binder. *Chem Sci (Camb)* 4:3673–3677.
24. Ai G, et al. (2015) Investigation of surface effects through the application of the functional binders in lithium sulfur batteries. *Nano Energy* 16:28–37.
25. Bhattacharya P, et al. (2016) Polyamidoamine dendrimer-based binders for high-loading lithium–sulfur battery cathodes. *Nano Energy* 19:176–186.
26. Su YS, Manthiram A (2012) Lithium-sulphur batteries with a microporous carbon paper as a bifunctional interlayer. *Nat Commun* 3:1166.
27. Chung S-H, Manthiram A (2014) Carbonized eggshell membrane as a natural polysulfide reservoir for highly reversible Li-S batteries. *Adv Mater* 26(9):1360–1365.
28. Gu X, et al. (2015) A porous nitrogen and phosphorous dual doped graphene blocking layer for high performance Li-S batteries. *J Mater Chem A* 3(32):16670–16678.
29. Li Z, Zhang JT, Chen YM, Li J, Lou XW (2015) Pie-like electrode design for high-energy density lithium-sulfur batteries. *Nat Commun* 6:8850.
30. Ma G, et al. (2014) Enhanced cycle performance of Li–S battery with a polypyrrole functional interlayer. *J Power Sources* 267:542–546.
31. Zhang K, et al. (2014) Nickel foam as interlayer to improve the performance of lithium–sulfur battery. *J Solid State Electrochem* 18(4):1025–1029.
32. Li W, et al. (2014) V_2O_5 polysulfide anion barrier for long-lived Li–S batteries. *Chem Mater* 26(11):3403–3410.
33. Han X, et al. (2013) Reactivation of dissolved polysulfides in Li–S batteries based on atomic layer deposition of Al_2O_3 in nanoporous carbon cloth. *Nano Energy* 2(6):1197–1206.
34. Zhubing X, et al. (2015) A lightweight TiO_2/graphene interlayer, applied as a highly effective polysulfide absorbent for fast, long-life lithium–sulfur batteries. *Adv Mater* 27(18):2891–2898.
35. Barchasz C, Leprêtre J-C, Alloin F, Patoux S (2012) New insights into the limiting parameters of the Li/S rechargeable cell. *J Power Sources* 199:322–330.
36. Deng Z, et al. (2013) Electrochemical impedance spectroscopy study of a lithium/sulfur battery: Modeling and analysis of capacity fading. *J Electrochem Soc* 160(4):A553–A558.
37. Liang X, et al. (2015) A highly efficient polysulfide mediator for lithium-sulfur batteries. *Nat Commun* 6:5682.
38. Yin L-C, et al. (2016) Understanding the interactions between lithium polysulfides and N-doped graphene using density functional theory calculations. *Nano Energy* 25:203–210.
39. Lucht BL, Bernstein MP, Remenar JF, Collum DB (1996) Polydentate amine and ether solvates of lithium hexamethyldisilazide (LiHMDS): Relationship of ligand structure, relative solvation energy, and aggregation state. *J Am Chem Soc* 118(44):10707–10718.
40. Rogers RD, Vann Bynum R, Atwood JL (1984) The crystal structure of LiBr·($CH_3OCH_2CH_2OCH_3$)$_2$. *J Crystallogr Spectrosc Res* 14(1):29–34.
41. Niecke E, Nieger M, Schmidt O, Gudat D, Schoeller WW (1999) Spectroscopic and structural characterization of a phosphavinylidene carbenoid, mes*-PC(Cl){Li(DME)$_2$}: Stabilization of a carbenanionic center by a cisoid lone pair interaction. *J Am Chem Soc* 121(3):519–522.
42. Clark DT, Feast WJ, Kilcast D, Musgrave WKR (1973) Applications of ESCA to polymer chemistry. III. Structures and bonding in homopolymers of ethylene and the fluoroethylenes and determination of the compositions of fluoro copolymers. *J Polym Sci Polym Chem Ed* 11(2):389–411.
43. Hoffmann EA, et al. (2005) Relation between C1s XPS binding energy and calculated partial charge of carbon atoms in polymers. *THEOCHEM* 725(1–3):5–8.